# The tethered peptide activation mechanism of adhesion GPCRs

**Document Version:**
Accepted author manuscript (peer-reviewed)

**Citation for published version:**
Barros-Álvarez, X, Nwokonko, RM, Vizurraga, A, Matzov, D, He, F, Papasergi-Scott, MM, Robertson, MJ, Panova, O, Yardeni, EH, Seven, AB, Kwarcinski, FE, Su, H, Peroto, MC, Meyerowitz, JG, Shalev-Benami, M, Tall, GG & Skiniotis, G 2022, 'The tethered peptide activation mechanism of adhesion GPCRs', *Nature (London)*, vol. 604, no. 7907, pp. 757-762. https://doi.org/10.1038/s41586-022-04575-7

*Total number of authors:*
17

**Digital Object Identifier (DOI):**
10.1038/s41586-022-04575-7

**Published In:**
Nature (London)

# The tethered peptide activation mechanism of adhesion GPCRs

Ximena Barros-Álvarez[1,*], Robert M. Nwokonko[1,*], Alexander Vizurraga[2,*], Donna Matzov[3,*], Feng He[1], Makaía M. Papasergi-Scott[1], Michael J. Robertson[1], Ouliana Panova[1], Eliane Hadas Yardeni[3], Alpay B. Seven[1], Frank E. Kwarcinski[2], Hongyu Su[2], Maria Claudia Peroto[1], Justin G. Meyerowitz[1], Moran Shalev-Benami[3,#], Gregory G. Tall[2,#], Georgios Skiniotis[1,4,#].

**Affiliations:**

[1] Department of Molecular and Cellular Physiology, Stanford University School of Medicine, Stanford, CA, USA

[2] Department of Pharmacology, University of Michigan School of Medicine, Ann Arbor, USA

[3] Department of Chemical and Structural Biology, Weizmann Institute of Science, Rehovot, Israel.

[4] Department of Structural Biology, Stanford University School of Medicine, Stanford, CA, USA

*These authors have contributed equally

#Correspondence: moransb@weizmann.ac.il
gregtall@med.umich.edu
yiorgo@stanford.edu

**Adhesion G protein-coupled receptors (aGPCRs) are characterized by the presence of auto-proteolysing extracellular regions (ECRs) involved in cell-cell and cell-extracellular matrix interactions[1]. Self-cleavage within the aGPCR auto-proteolysis-inducing (GAIN) domain produces two protomers, N-terminal and C-terminal fragments (NTF and CTF), that remain non-covalently attached after receptors reach the cell surface[1]. Upon NTF dissociation, the C-terminus of the GAIN domain acts as a tethered agonist (TA) peptide to activate the 7-transmembrane (7TM) domain with a mechanism that has been poorly understood[2-5]. Here we provide cryo-EM snapshots of two distinct members of the**

**aGPCR family, GPR56 and Latrophilin-3 (LPHN3). Low resolution maps of the receptors in their NTF-bound state indicate that the GAIN domain projects flexibly towards the extracellular space, keeping the encrypted TA peptide away from the 7TM. High resolution structures of GPR56 and LPHN3 in their active, G protein-coupled states, reveal that after ECR dissociation, the decrypted TA peptides engage the 7TM core with a remarkable conservation of interactions that also involve extracellular loop 2 (ECL2). TA binding stabilizes breaks in the middle of TM6 and TM7 that facilitates aGPCR coupling and activation of heterotrimeric G proteins. Collectively, these results enable us to propose a general model for aGPCR activation.**

Adhesion GPCRs (Family B2) contain extracellular regions (ECRs) that participate in cellular communication to regulate cell size, shape, polarity, adhesion, migration, cycle, death and differentiation[6]. The ECRs include diverse sets of adhesion domains and a conserved GAIN domain responsible for self-cleaving the receptor into the NTF that binds to extracellular components and the CTF or 7TM domain that couples to G proteins. Cleavage occurs intracellularly during protein maturation, and the two fragments remain non-covalently attached after presentation at the cell surface[7]. ECR dissociation through prospective force-based mechanisms mediated by binding to extracellular partners is followed by 7TM rearrangements that lead to G protein activation[8].

GPR56 (ADGRG1) and LPHN3 (ADGRL3) are two distinct aGPCRs involved in diverse physiological processes[9]. GPR56 is widely distributed and implicated in immune system functions, hemostasis, brain development, muscle function and male fertility [10]. Besides the GAIN domain, the GPR56 ECR consists of a PLL (Pentraxin/Laminin/neurexin/sex-hormone-binding-globulin-Like) domain critical for protein ligand binding during oligodendrocyte development[11]. Dysregulation of GPR56 is associated with cancers[12-14] and cortical brain malformation disorders, including bilateral frontoparietal polymicrogyria (BFPP)[11,15]. In neural stem cells and platelets, GPR56 is activated by its extracellular matrix ligand, collagen III, and signals through the $G_{12/13}$ family of G proteins[16,17]. In contrast, LPHN3 is primarily abundant in the central nervous system (CNS), where it interacts with several *trans*-cellular signaling proteins, including teneurins (TENs) and fibronectin-like domain containing leucine-rich transmembrane proteins (FLRTs)[9,18,19] that are critical for the maintenance of the synaptic architecture. Besides its GAIN domain, the LPHN3 ECR consists of a lectin binding domain (LEC), an olfactomedin-like domain (OLF) that contribute to its cell-cell adhesive properties[9,18,19], and a hormone binding domain (HormR) resembling the typical hormR domain of Family B1 GPCRs. LPHN3 is proposed to mediate its neuronal functions mainly through $G_{12/13}$ protein coupling and signaling through the Rho/Rac pathway, leading to actin cytoskeletal changes[1,20,21]. Notably, LPHN3 has been linked to substance abuse and attention deficit hyperactivity disorder (ADHD), elevating its interest as a potential pharmacological target[22].

Crystal structures have shown the architecture of the LPHN1 GAIN and HormR domains[23], the LPHN3 OLF and LEC domains in complex with FLRT[24-26], and the entire ECR of GPR56[11]. A recent cryo-EM study showed the structure of the aGPCR GPR97/miniG$_o$ complex as stabilized by partial agonist glucocorticoids[27]. Notably, however, the mechanism of aGPCR activation by the native tethered agonist (TA) peptide remains elusive. Here we describe the structures of GPR56 and LPHN3 in their fully active, G protein-coupled states bound intramolecularly to their native TA peptides. Complemented by low-resolution cryo-EM visualization of NTF-bound holoreceptors, functional assays, and molecular dynamics (MD) simulations, the results provide a structural framework for aGPCR activation and G protein recruitment.

## GPR56 and LPHN3 display flexible ECRs

We first sought to examine the NTF-bound (TA-encrypted; Fig. 1a) structures of human GPR56 and LPHN3 by cryo-EM. For LPHN3, we purified recombinant receptor including the N-terminal HormR and GAIN domains bound non-covalently to the 7TM after self-cleavage at the native G protein proteolytic site (GPS) (Extended Data Fig. 1). Because purified full-length auto-proteolysed GPR56 underwent spontaneous ECR dissociation, we employed an autoproteolytically-deficient GPR56 H381S GPS mutant holoreceptor (Extended Data Fig. 2). For both GPR56 and LPHN3, cryo-EM visualization allowed us to obtain 3D reconstructions only at low resolution (Fig. 1b-c; Extended Data Figs. 1 and 2), primarily due to the continuous flexibility of the ECRs. This flexibility was particularly evident in LPHN3 (Fig. 1b and Extended Data Fig. 1f), presumably because the stalk connecting the GAIN domain to the 7TM is extended by two amino acids compared to the GPR56 stalk, accounting for a ~6Å increase in length. LPHN3 embedded in lipid nanodiscs exhibited the same behaviour (Extended Data Fig. 1g-i), indicating that the detergent micelle did not perturb putative interactions between the GAIN and 7TM domain. Collectively, these results showed that in the NTF-bound state, the GAIN domain is not ordered against the 7TM, presumably allowing the ECR the flexibility to sample protein/ligand binding partners in the extracellular space.

## Structures of active-state GPR56 and LPHN3 in complex with $G_{13}$

For structural studies of activated GPR56 and LPHN3 in their TA-bound states coupled to G protein, we created constructs consisting of the unencrypted peptide agonists followed by the stalk linker and the 7TM domain, thus mimicking aGPCR CTFs (Figs. 1d, 2a and Extended Data Fig. 3a). Inspired by the engineering of a thermostable $\text{miniG}_{\alpha12}$[28], we designed a mini-G protein variant of the $G_{13}$ α subunit (Extended Data Fig. 3a-b). Co-expression of receptors and $\text{miniG}_{13}$ heterotrimer enabled us to isolate stable complexes (Extended Data Fig. 3c) and obtain cryo-EM maps of GPR56/$\text{miniG}_{13}$ and LPHN3/$\text{miniG}_{13}$ (Fig. 1e-f). Combinations of local refinements of the 7TM domain and G protein yielded maps with nominal resolutions of 2.7 Å and 2.9 Å for

GPR56, and 2.9 Å and 3.1 Å for the LPHN3 complexes, respectively (Extended Data Table 1 and Extended Data Figs. 4 and 5).

## Tethered-peptide-agonist interactions with the 7TM

The stalks of aGPCRs are ~20-24 residue N-terminal extensions of TM1, with the first ~7 amino acids comprising the TA (Fig. 2a). Both GPR56/ and LPHN3/G protein complex maps revealed well-resolved densities for the native TA peptides bound within the orthosteric site of the 7TM bundle (Fig. 2), in agreement with the proposed tethered-peptide-agonist model[1]. In this configuration, the stalks bend nearly 180º downward into the core of the 7TM (Figs. 2b-d and 3 a-b), permitting the TAs to engage a remarkable set of conserved interactions, predominantly with TMs 1, 2, 6, 7 and extracellular loop 2 (ECL2) (Figs. 2 and 3, Extended Data Table 2).

The observed interactions were assessed with G protein activation assays using plasma membrane-enriched isolates from cells overexpressing mutant receptors (Fig. 3c-d). We note that relative receptor levels were measured using the same membrane isolates and do not represent direct measurement of cell surface receptor levels. To assess surface expression, we employed a cell surface biotinylation/pulldown experiment for two of the most activity-defective mutants ($W^{7.42}$A and $F^{2.64}$A, described below), which showed that targeted mutations did not substantially impact receptor trafficking to the plasma membrane (Fig. 3, Extended Data Figs. 6-8, Extended Data Table 3 and Supplementary Data Table 1).

The third residue of most aGPCR TAs is a highly conserved phenylalanine (F385 in GPR56 and F844 in LPHN3) required for TA-stimulated $G_{13}$ activation (Fig. 3a-d; Extended Data Figs. 6 and 7)[4]. GPR56 F385 interacts with $C411^{1.47}$ and forms a hydrophobic interaction with $F454^{2.64}$ (Fig. 3a) (Wooten numbering in superscript [29], equivalent to the Ballesteros-Weinstein numbering for Family A GPCRs [30]). Likewise, LPHN3 TA residue F844 interacts with $I872^{1.47}$ and $F914^{2.64}$ (Fig. 3b and 3d). The interaction with $C411^{1.47}$ was dispensable for G protein activation by GPR56, but the hydrophobic interactions of either TA phenylalanine with $F^{2.64}$ are essential, as demonstrated by the near complete loss of $G_{13}$ activation by GPR56 $F454^{2.64}A$ or LPHN3 $F914^{2.64}A$ mutants (Fig. 3c-d).

Another set of critical interactions were observed between the TA and ECL2 that reaches into the interior of the 7TM domain to form a wedge-like plug structure (Fig. 3e-f; Extended Data Fig. 8a-b). ECL2 residues GPR56 $W557^{45.51}$ and LPHN3 $W1000^{45.51}$ reside within hydrophobic 7TM patches ($L476^{3.36}$ and $I558^{45.52}$ in GPR56 or $L934^{3.36}$, $L1001^{45.52}$ and $I1008^{5.36}$ in LPHN3) and interact with the sixth TA residue, a conserved leucine (GPR56 L388 or LPHN3 L847) (Fig. 3e-f). Interestingly, $W421^{45.51}$ in the ECL2 of GPR97 (ADGRG3; PDB ID: 7D76, 7D77) also reaches down into the 7TM interior close to the bound glucocorticoid ligand[27]. Our assays show that these interactions are essential for tethered agonism, as the GPR56 $W557^{45.51}A$ and LPHN3 $W1000^{45.51}A$ mutants had negligible ability to activate $G_{13}$ (Fig. 3c-d; Extended Data Figs. 6 and 7). Notably, ECL2 assumes a stable configuration due, in part, to the presence of a disulfide bond between TM3 residue $C^{3.29}$ and ECL2 residue $C^{45.50}$, adjacent to $W^{45.51}$ that coordinates the binding of TA L388/L847. We postulate that the decrypted TA peptide needs to be flexible to thread through a relatively narrow opening at the extracellular face of the receptor and interact with multiple residues of the orthosteric binding site. In support of this notion, MD simulations of the TA peptide alone in solution showed that it did not assume the conformation observed in the orthosteric binding site, but was instead conformationally variable without adopting a secondary structure (Extended Data Fig. 9a-b).

Our examination of the activity of GPR56 M389A and LPHN3 M848A mutants (Fig. 3c-d) reaffirmed that mutation of this conserved seventh TA residue critically reduced G protein stimulation by GPR56 or GPR110[4]. In the TA-bound structures, GPR56 M389 and LPHN3 M848 interact with GPR56 $I620^{6.56}$ and LPHN3 $L1072^{6.57}$, respectively, (Fig. 3e-f), and mutation of either residue moderately reduced receptor-stimulated $G_{13}$ activation (Fig. 3c-d). More importantly, in both LPHN3 and GPR56, the TA seventh methionine interacts with $W^{6.53}$ (Extended Data Fig. 8c-d), a conserved residue that interacted with the bound steroid ligand in the GPR97 partial agonist-activated receptor structure[27]. The function of the aGPCR $W^{6.53}$ seems to parallel the Family A GPCR “toggle switch” residue $W^{6.48}$ [31], which rearranges upon agonist binding and drives the opening of the cytoplasmic end of TM6, thereby enabling G protein engagement. In agreement with this role, mutation of $W^{6.53}$ in GPR56 (W617A) or LPHN3 (W1068A) strongly abrogated receptor-dependent G protein activation (Fig. 3c-d).

## Active state conformation of the GPR56 and LPHN3 7TM bundles

Even though GPR56 and LPHN3 belong to different aGPCR subfamilies, their TA-bound 7TM conformations were remarkably similar (Extended Data Fig. 8e). On the extracellular side of both active-state receptors, TM1 is bent towards the transmembrane bundle presumably by TA agonist stabilization within the 7TM domain (Fig. 3g). TM7 is bent outwards, accommodating both the TA and the portion of ECL2 that reaches down into the orthosteric binding site (Extended Data Fig. 8a-b). Residue $G^{7.50}$ (G645 of GPR56 and G1094 of LPHN3) acts as a pivot point to kink TM7, which parallels the reported kinked TM7 arrangements of active Family B1 GPCRs[32-34] (Extended Data Fig. 10a-b). Accompanying TM7, TM6 is kinked outwards at the hinge residue $G^{6.50}$, three residues from toggle switch $W^{6.53}$. The intracellular halves of GPR56 and LPHN3 TM5 and TM6 are in an open conformation, as expected for fully activated G protein-bound states. Notably, the degree of TM6 opening and the kink at residue 6.50 is distinct compared to the glucocorticoid-bound GPR97/mini$G_o$ complex (Extended Data Fig. 10c,g), where TM6 appeared to open more modestly without a kink[27]. This difference, along with the lack of cytoplasmic opening of TM7 in the GPR97/mini$G_o$ structure, may reflect that the tethered-peptide acts as a full agonist while the corticoids are partial agonists that stabilize an intermediate active state[35].

Interestingly, residue $Q^{7.49}$ establishes an electrostatic interaction with the indole nitrogen of the toggle switch $W^{6.53}$, stabilizing the joint extracellular opening of the transmembrane helices and the hydrophobic core of the receptors (Extended Data Fig. 8c-d). The core of both receptors comprises a network of residues that interact with the methionine TA seventh residue through $W^{6.53}$, which is coordinated by $M487^{3.47}$ and $F637^{7.42}$ in GPR56 or $M945^{3.47}$, $F942^{3.44}$ and $F1086^{7.42}$ in LPHN3, as well as the aforementioned electrostatic interactions involving $Q^{7.49}$ (Fig. 3e-f, Extended Data Fig. 8c-d, f).

## aGPCR interactions with $G_{13}$

GPR56 and LPHN3 engage the G protein somewhat differently, as evidenced by the 12° rotation between the N-terminal α-helices (αN) in the coupled $G_{13}$ α subunit (Extended Data Fig. 10d). Superposition of the Cα atoms of Gα of $miniG_{13}$ bound to GPR56 with $miniG_o$ coupled to 5HT1B (PDB ID: 6G79)[36] shows an RMSD of 1.54 Å, reflecting an overall conformational similarity between these receptor-coupled G proteins (Extended Data Fig. 10e). As observed in Family A and B1 GPCRs, the intracellular ends of TM5 and TM6 in the GPR56/$miniG_{13}$ and LPHN3/$miniG_{13}$ complexes are present in open conformations that accommodate binding of the G protein C-terminal α5 helix (Figs. 2 and 4a). While many side chain interactions between 7TM elements and the α5 helix are conserved between GPR56 and LPHN3 (Fig. 4b-c), we observed a notable difference with GPR56 TM2, which is closer to the α5 helix, resulting in the positioning of TM7 closer to TM6 (Fig. 4a). In effect, GPR56 residue $D434^{2.44}$ of TM2 establishes a hydrogen bond interaction with $G\alpha_{13}$ residue $Q226^{H5.22}$ not observed at the equivalent LPHN3 TM2 position (Fig. 4b-c). Consistent with this observation, the GPR56 D434A mutant had markedly reduced receptor-stimulated $G_{13}$ activation (Extended Data Figs. 6e and 7a).

The structures also reveal interactions between aGPCR ICL2 residues and the G protein N-terminal αN helix. $G_{\alpha 13}$ residues K27$^{\alpha N.51}$, T28$^{\alpha N.52}$ and R32$^{hns1.03}$ engage Y505$^{ICL2}$ of GPR56, whereas T28$^{\alpha N.52}$ and R32$^{hns1.03}$ establish polar interactions with backbone α-carbonyls of LPHN3 ICL2 E961 and E963, respectively. Additionally, GPR56 F502$^{ICL2}$ and the conserved LPHN3 residue F960$^{ICL2}$ establish hydrophobic interactions with multiple G protein residues, including a Pi-Pi interaction with mini$G_{\alpha 13}$ α5 helix residue F212$^{\alpha 5.08}$ (Fig. 4d-e). The substantially reduced abilities of GPR56 F502A and LPHN3 F960A mutants to activate $G_{13}$ supports the importance of these interactions (Extended Data Figs. 6e-f and 7).

Our MD simulations of active state LPHN3 without bound G protein provide a glimpse into the dynamics of ICL2. Comparing the difference in root mean square fluctuations (RMSF) in the final 100 ns of 1 μs trajectories between five replicate simulations with and without the TA reveals that in the absence of the TA, the half of ICL2 near TM5 becomes more flexible (Extended Data Fig. 9c-d), suggesting that tethered agonist binding to the 7TM domain stabilizes the ICL2 conformation.

## Model for tethered agonist mechanism of activation of aGPCRs

Dissociation of NTFs from aGPCRs unveils the TA peptide so that it may activate the 7TM by a mechanism that has been poorly understood[1]. Numerous studies have detected isolated aGPCR NTFs in a variety of tissues, suggesting that their presence is a remnant of an activation event or a result of spontaneous NTF shedding[1,7]. An activation mechanism with parallels has been described for protease-activated GPCRs (PAR1-4)[37,38], in which cleavage of the N-terminal leader sequences by exogenous proteases exposes a tethered peptide that serves to activate the receptor, although PAR TAs do not share sequence similarity with aGPCR TAs. Crystal structures of GPR56[11] and LPHN1[23] ECRs in complex with their cleaved TAs showed that the peptides fold as β-strands encrypted within the core of the GAIN$_B$ subdomain. Our NTF-bound structures illustrate that in the context of the holoreceptor, the GAIN domain is not anchored to the 7TM, thus keeping the TA encrypted and at a distance from the 7TM bundle (Extended Data Fig. 1e-f). In the TA-activated state structures, the decrypted TA penetrates the 7TM orthosteric binding pocket where it adopts a partial α-helical fold to stabilize an active receptor conformation (Fig. 2). Our MD simulations show that the peptide on its own is flexible and adopts minimal secondary structure (Extended Data Fig. 9a-b), indicating that the TA conformations observed in the X-ray studies and our current cryo-EM study are stabilized by interactions with the GAIN domain or the 7TM, respectively. This conformational adaptability appears to be a key component underlying the encryption/decryption of the TA and its agonistic properties for aGPCRs. The remarkable conservation of TA peptide interactions and 7TM conformation, including the role of ECL2, observed for two active-state aGPCRs from distinct subfamilies suggests that the structural determinants of receptor activation by the tethered agonist may be universal to aGPCRs, a hypothesis that will be further tested in future studies of additional aGPCRs in complex with different G protein partners.

## References

1 Vizurraga, A., Adhikari, R., Yeung, J., Yu, M. & Tall, G. G. Mechanisms of adhesion G protein–coupled receptor activation. *Journal of Biological Chemistry* **295**, 14065-14083, doi:https://doi.org/10.1074/jbc.REV120.007423 (2020).

2 Liebscher, I. *et al.* A tethered agonist within the ectodomain activates the adhesion G protein-coupled receptors GPR126 and GPR133. *Cell Rep* **9**, 2018-2026, doi:10.1016/j.celrep.2014.11.036 (2014).

3 Stoveken, H. M. *et al.* Dihydromunduletone Is a Small-Molecule Selective Adhesion G Protein-Coupled Receptor Antagonist. *Mol Pharmacol* **90**, 214-224, doi:10.1124/mol.116.104828 (2016).

4 Stoveken, H. M., Hajduczok, A. G., Xu, L. & Tall, G. G. Adhesion G protein-coupled receptors are activated by exposure of a cryptic tethered agonist. *Proc Natl Acad Sci U S A* **112**, 6194-6199, doi:10.1073/pnas.1421785112 (2015).

5 Wilde, C. *et al.* The constitutive activity of the adhesion GPCR GPR114/ADGRG5 is mediated by its tethered agonist. *FASEB J* **30**, 666-673, doi:10.1096/fj.15-276220 (2016).

6 Hamann, J. *et al.* International Union of Basic and Clinical Pharmacology. XCIV. Adhesion G protein-coupled receptors. *Pharmacol Rev* **67**, 338-367, doi:10.1124/pr.114.009647 (2015).

7 Langenhan, T., Aust, G. & Hamann, J. Sticky signaling--adhesion class G protein-coupled receptors take the stage. *Sci Signal* **6**, re3, doi:10.1126/scisignal.2003825 (2013).

8 Langenhan, T., Piao, X. & Monk, K. R. Adhesion G protein-coupled receptors in nervous system development and disease. *Nat Rev Neurosci* **17**, 550-561, doi:10.1038/nrn.2016.86 (2016).

9 Boucard, A. A., Maxeiner, S. & Südhof, T. C. Latrophilins function as heterophilic cell-adhesion molecules by binding to teneurins: regulation by alternative splicing. *The Journal of biological chemistry* **289**, 387-402, doi:10.1074/jbc.M113.504779 (2014).

10 Jin, Z., Luo, R. & Piao, X. in *G Protein-Coupled Receptors in Health and Disease, Pt B* Vol. 89 *Progress in Molecular Biology and Translational Science* (ed Y. X. Tao) 1-13 (2009).

11 Salzman, G. S. *et al.* Structural Basis for Regulation of GPR56/ADGRG1 by Its Alternatively Spliced Extracellular Domains. *Neuron* **91**, 1292-1304, doi:10.1016/j.neuron.2016.08.022 (2016).

12 Purcell, R. H. & Hall, R. A. Adhesion G Protein-Coupled Receptors as Drug Targets. *Annu Rev Pharmacol Toxicol* **58**, 429-449, doi:10.1146/annurev-pharmtox-010617-052933 (2018).

13 Aust, G., Zhu, D., Van Meir, E. G. & Xu, L. Adhesion GPCRs in Tumorigenesis. *Handbook of experimental pharmacology* **234**, 369-396, doi:10.1007/978-3-319-41523-9_17 (2016).

14 Scholz, N. Cancer Cell Mechanics: Adhesion G Protein-coupled Receptors in Action? *Frontiers in oncology* **8**, 59, doi:10.3389/fonc.2018.00059 (2018).

15 Piao, X. *et al.* G protein-coupled receptor-dependent development of human frontal cortex. *Science* **303**, 2033-2036, doi:10.1126/science.1092780 (2004).

16 Iguchi, T. *et al.* Orphan G protein-coupled receptor GPR56 regulates neural progenitor cell migration via a G alpha 12/13 and Rho pathway. *The Journal of biological chemistry* **283**, 14469-14478, doi:10.1074/jbc.M708919200 (2008).

17 Luo, R. *et al.* G protein-coupled receptor 56 and collagen III, a receptor-ligand pair, regulates cortical development and lamination. *Proc Natl Acad Sci U S A* **108**, 12925-12930, doi:10.1073/pnas.1104821108 (2011).

18 Sando, R., Jiang, X. & Südhof, T. C. Latrophilin GPCRs direct synapse specificity by coincident binding of FLRTs and teneurins. *Science* **363**, eaav7969, doi:10.1126/science.aav7969 (2019).

19 Li, J. *et al.* Structural Basis for Teneurin Function in Circuit-Wiring: A Toxin Motif at the Synapse. *Cell* **173**, 735-748.e715, doi:10.1016/j.cell.2018.03.036 (2018).

20 Mathiasen, S. *et al.* G12/13 is activated by acute tethered agonist exposure in the adhesion GPCR ADGRL3. *Nature Chemical Biology* **16**, 1343-1350, doi:10.1038/s41589-020-0617-7 (2020).

21 Cruz-Ortega, J. S. & Boucard, A. A. Actin cytoskeleton remodeling defines a distinct cellular function for adhesion G protein-coupled receptors ADGRL/latrophilins 1, 2 and 3. *Biology Open* **8**, doi:10.1242/bio.039826 (2019).

22 Wallis, D. *et al.* Initial characterization of mice null for Lphn3, a gene implicated in ADHD and addiction. *Brain Res* **1463**, 85-92, doi:10.1016/j.brainres.2012.04.053 (2012).

23 Araç, D. *et al.* A novel evolutionarily conserved domain of cell-adhesion GPCRs mediates autoproteolysis. *Embo j* **31**, 1364-1378, doi:10.1038/emboj.2012.26 (2012).

24 Lu, Y. C. *et al.* Structural Basis of Latrophilin-FLRT-UNC5 Interaction in Cell Adhesion. *Structure* **23**, 1678-1691, doi:10.1016/j.str.2015.06.024 (2015).

25 Jackson, V. A. *et al.* Structural basis of latrophilin-FLRT interaction. *Structure* **23**, 774-781, doi:10.1016/j.str.2015.01.013 (2015).

26 Jackson, V. A. *et al.* Super-complexes of adhesion GPCRs and neural guidance receptors. *Nature Communications* **7**, 11184, doi:10.1038/ncomms11184 (2016).

27 Ping, Y.-Q. *et al.* Structures of the glucocorticoid-bound adhesion receptor GPR97–Go complex. *Nature* **589**, 620-626, doi:10.1038/s41586-020-03083-w (2021).

28 Nehmé, R. *et al.* Mini-G proteins: Novel tools for studying GPCRs in their active conformation. *PLOS ONE* **12**, e0175642, doi:10.1371/journal.pone.0175642 (2017).

29 Wootten, D., Simms, J., Miller, L. J., Christopoulos, A. & Sexton, P. M. Polar transmembrane interactions drive formation of ligand-specific and signal pathway-biased family B G protein-coupled receptor conformations. *Proceedings of the National Academy of Sciences* **110**, 5211, doi:10.1073/pnas.1221585110 (2013).

30 Ballesteros, J. A. & Weinstein, H. in *Methods in Neurosciences* Vol. 25 (ed Stuart C. Sealfon) 366-428 (Academic Press, 1995).

31 Weis, W. I. & Kobilka, B. K. The Molecular Basis of G Protein–Coupled Receptor Activation. *Annual Review of Biochemistry* **87**, 897-919, doi:10.1146/annurev-biochem-060614-033910 (2018).

32 Zhang, Y. *et al.* Cryo-EM structure of the activated GLP-1 receptor in complex with a G protein. *Nature* **546**, 248-253, doi:10.1038/nature22394 (2017).

33 Hilger, D. *et al.* Structural insights into differences in G protein activation by family A and family B GPCRs. *Science* **369**, eaba3373, doi:doi:10.1126/science.aba3373 (2020).

34 Liang, Y.-L. *et al.* Phase-plate cryo-EM structure of a class B GPCR-G-protein complex. *Nature* **546**, 118-123, doi:10.1038/nature22327 (2017).

35 Stoveken, H. M., Larsen, S. D., Smrcka, A. V. & Tall, G. G. Gedunin- and Khivorin-Derivatives Are Small-Molecule Partial Agonists for Adhesion G Protein-Coupled Receptors GPR56/ADGRG1 and GPR114/ADGRG5. *Molecular Pharmacology* **93**, 477-488, doi:10.1124/mol.117.111476 (2018).

36 García-Nafría, J., Nehmé, R., Edwards, P. C. & Tate, C. G. Cryo-EM structure of the serotonin 5-HT(1B) receptor coupled to heterotrimeric G(o). *Nature* **558**, 620-623, doi:10.1038/s41586-018-0241-9 (2018).

37 Macfarlane, S. R., Seatter, M. J., Kanke, T., Hunter, G. D. & Plevin, R. Proteinase-Activated Receptors. *Pharmacological Reviews* **53**, 245-282 (2001).

38 Vu, T. K., Hung, D. T., Wheaton, V. I. & Coughlin, S. R. Molecular cloning of a functional thrombin receptor reveals a novel proteolytic mechanism of receptor activation. *Cell* **64**, 1057-1068, doi:10.1016/0092-8674(91)90261-v (1991).

## Figure legends

**Fig. 1 | Cryo-EM reconstructions for GPR56 and LPHN3. a**, Cartoon representation of a self-cleaved NTF-bound aGPCR. The encrypted tethered agonist (TA, orange) resides in a β-strand conformation within the core of the GAIN domain. **b, c,** Low resolution maps for NTF-bound state receptors showing flexibility of the ECR. Side and top views of **b,** LPHN3 (magenta) and **c,** GPR56 (blue). Maps are the result of 3D classification, with three distinct classes of LPHN3 superimposed. Dashed arrows indicate NTF mobility. **d,** Interactions of the NTF with extracellular partners are proposed to result in its dissociation from the CTF, thereby decrypting the TA peptide in the extracellular space. Binding of the TA within the 7TM domain (CTF) orthosteric site stabilizes an active receptor conformation that induces G protein nucleotide exchange and elicits intracellular signaling. **e, f,** High resolution maps for active GPR56 and

LPHN3 complexes with G protein. The micelle-embedded 7TM domains are coupled to miniG$_{13}$ heterotrimer. The cryo-EM maps have been assigned and colored accordingly. In **b-f,** scale bars are indicated.

**Fig. 2 | Structures of active GPR56 and LPHN3 complexes with bound tethered agonist (TA) peptide. a,** Decrypted TA sequence for GPR56 on the left (cyan) and LPHN3 on the right (pink), stalk linker sequences are underlined in black and followed by the 7TM starting with the first TM1 residue V$^{1.34}$. **b,** Model for active tethered agonist-bound GPR56/miniG$_{13}$ complex with box around the tethered agonist binding site (left) and cryo-EM density and model for the TA peptide (right). **c,** Model for active tethered agonist-bound LPHN3/miniG$_{13}$ complex with box around the tethered agonist binding site (right) and cryo-EM density and model for the TA peptide (left). **d,** Top-down views of active GPR56/ (left) and LPHN3/miniG$_{13}$ (right) complexes. Black arrows point to the tethered agonist bound to the 7TM domains and to the stalk linkers emanating from TM1.

**Fig. 3 | Tethered-peptide-agonist interactions. a, b,** Tethered agonist (TA) interactions with TM1 and TM2 in **a,** GPR56 and **b,** LPHN3. **c ,d,** Activation of reconstituted G$_{13}$ via GTPγS binding activity assay by TA and TA-interacting mutants for **c,** GPR56 and **d,** LPHN3**.** Data displayed as average of n = 3 biologically-independent reactions with error bars representing ± S.D. Statistical significance between mutant and wild-type receptors was calculated using RM one-way ANOVA analysis, n.s. = not significant, * = $p < 0.05$, ** = $p < 0.01$. Further detailed statistical information can be found in Supplementary Data Table 1. **e, f,** TA interactions with ECL2 and the hydrophobic core in **e,** GPR56 and **f,** LPHN3**.** GPR56 7TM in blue and TA in cyan, LPHN3 7TM in magenta and TA in pink. g, Top view of superposition with GPR97 (PDB ID: 7D77, in white) showing helix rearrangements for TM1, TM6 and TM7 when compared to TA-bound-GPR56 (blue) and -LPHN3 (magenta) and cortisol ligand (carbon atoms in green)-

bound GPR97, showing that the cortisol or TA ligands occupy a common orthosteric site within the three receptors.

**Fig. 4 | G protein binding by GPR56 and LPHN3. a,** G protein binding through the mini-$G_{13}$ α5 helix (α5) with superimposed GPR56 (blue) and LPHN3 (magenta). **b,** mini-$G_{13}$ α5 helix (α5) interactions with GPR56 and **c,** LPHN3. Many of these interactions are conserved. TM3 (L494$^{3.54}$ and L497$^{3.57}$), TM5 (M586$^{5.57}$, I590$^{5.61}$ and R592$^{5.63}$), TM6 (T605$^{6.41}$), and TM7 (M655$^{7.60}$) of GPR56, and TM3 (M955$^{3.57}$ and L956$^{3.58}$), TM5 (M1033$^{5.61}$), TM6 (S1052$^{6.37}$ and I1055$^{6.40}$) and TM7 (Q1105$^{7.61}$) of LPHN3 establish hydrophobic or polar interactions with the $G\alpha_{13}$ α5 helix. **d,** ICL2 interactions with the mini-$G_{13}$ N-terminal helix (αN) for GPR56 and e, LPHN3. G protein residues labeled in gold, receptor residues labeled in black, hydrogen bond interactions are dashed grey lines.

## Methods

### Construct design, cloning and virus production of aGPCRs

For the structural and biochemical studies of aGPCRs in their NTF-bound form, the full-length sequence of human *GPR56* (*ADGRG1*) (Isoform 2, Uniprot ID: Q9Y653-2) and LPHN3 (ADGRL3) (Isoform 1, Uniprot ID: Q9HAR2-1, residues 495-1138) were cloned into pFastBac1™ (ThermoFisher) following an N-terminal hemagglutinin (HA)-membrane targeting signal peptide and a FLAG-tag (for LPHN3, the tag was also flanked by a Tobacco Etch Virus nuclear-inclusion-a endopeptidase (TEV) protease - cleavage site). For GPR56, a cleavage-deficient GPR56 H381S GPS mutant was employed to prevent autoproteolysis and dissociation of the N- and C-terminal GPR56 fragments during purification.

For the active-state constructs, truncated versions comprising the 7TM domain and the tethered agonist peptide sequences corresponding to residues 383-687 and 842-1138 of GPR56 and

LPHN3, respectively, were cloned into pFastBac1™. The ORFs were inserted following an N-terminal HA-membrane targeting signal peptide and supplemented with an additional methionine residue that was found to be important for the efficient signal peptide cleavage in our preliminary studies (data not shown). The GPR56 expression constructs included either a 6X or a 10X C-terminal histidine tag preceded by a Human Rhinovirus (HRV) 3C Protease cleavage site. The LPHN3 expression constructs included a green fluorescent protein (GFP) module located between the 3C cleavage site and the C-terminal 6X histidine tag. A schematic description of the constructs used in this study is provided in Extended Data Figs. 1-3.

Baculovirus production was conducted using the Bac-to-Bac system (ThermoFisher). Viruses were prepared according to manufacturer's instructions in *Spodoptera frugiperda* 9 (*Sf9*) cells grown in ESF921 medium (Expression systems LLC).

### Construct design and cloning of the miniG$_{13}$ heterotrimer

The miniG$_{\alpha13}$ generated in this study was inspired by the design of miniG$_{\alpha12}$ described in Nehmé *et al* [28]. The alpha helical domain of human G$_{\alpha13}$ (residues D253$^{S4H3.05}$ through T262$^{S4H3.14}$) was replaced by a GGSGGSGG linker, and the stabilizing mutations G57D$^{S1H1.03}$, E58N$^{S1H1.04}$, S248D$^{S4.07}$, E251D$^{S4H3.03}$, I271D$^{H3.08}$, I355A$^{H5.04}$ and V358I$^{H5.07}$ were introduced (Extended Data Fig. 3b). In addition, residues 1-30 were replaced by the first 15 N-terminal residues of G$_{\alpha i2}$ to improve expression and purification while maintaining interaction with the receptor (Extended Data Fig. 10f). As described for miniG$_q$[39], the miniG$_{\alpha13/i}$ sequence was cloned into the P10 promoter cloning site in pFastBac™ Dual (Invitrogen) and fused downstream of a human G$_{\gamma2}$ gene that was separated by a 3X GSA (Gly/Ser/Ala) linker. Human G$_{\beta1}$ including an N-terminal 6X histidine tag and Human rhinovirus 3C protease signal sequence was inserted into the second cloning site after the polyhedrin promoter (Extended Data Fig. 3a). The pFastBac™ Dual vector allows for the bicistronic gene expression, and was utilized to form the heterotrimeric G protein complex *in situ*.

## Protein expression and purification

### *Purification of NTF-bound aGPCR holoreceptors in detergents*

Proteins were expressed in *Sf9* cells at 27°C and were harvested 48 h post viral infection. Cell pellets were lysed in a buffer containing 20 mM Tris pH 7.5, 1 mM EDTA, 15% v/v glycerol, 1 mM PMSF, 160 µg/mL benzamidine, 2.5 µg/mL leupeptin and 2 mg/mL iodoacetamide for 1h at 4°C. Membranes were harvested through centrifugation at 37,000 × g for 30 min and homogenized in 0.5% (w/v) lauryl maltose neopentyl glycol (LMNG, Anatrace) and 0.1% (w/v) cholesteryl hemisuccinate (CHS, Anatrace) in solubilization buffer (20 mM HEPES pH 7.5, 150 mM NaCl, 15% v/v glycerol, 1 mM PMSF, 160 µg/mL benzamidine, 2.5 µg/mL leupeptin, benzonase and 1 mg/mL iodoacetamide). Insoluble material was removed by centrifugation at 37,000 × g for 30 min. Detergent solubilized receptors were purified by affinity capture, with Ni chelate resin capture for the uncleavable GPR56, and double anti-FLAG / Ni chelate resin capture for LPHN3 that was applied to ensure the purification of the intact protein containing both the N- and C- termini, which are not covalently attached.

Solubilized GPR56 was supplemented with 10 mM imidazole and loaded onto a TALON Metal Affinity Resin (Takara) column. The column was washed with 20 mM HEPES, pH 7.5, 150 mM NaCl, 10% v/v glycerol, 2 mM $MgCl_2$, 10 mM imidazole, 0.1% (w/v) LMNG, 0.02% (w/v) glyco-diosgenin (GDN, Anatrace), 0.01% (w/v) CHS. The protein was eluted with 20 mM HEPES, pH 7.5, 150 mM NaCl, 10% v/v glycerol, 2 mM $MgCl_2$, 200 mM imidazole, 0.01% (w/v) LMNG, 0.002% (w/v) GDN, 0.001% (w/v) CHS. HRV 3C Protease was added and incubated at 4°C for 16h while the sample was simultaneously dialyzed against low imidazole buffer. The cleaved sample was then loaded onto a TALON resin and the flow through was collected and concentrated using an Amicon Ultra Centrifugal Filter (MWCO 100kDa, Merck-Millipore).

For LPHN3 the clarified supernatant was incubated with an Anti-DYKDDDDK G1 Affinity Resin (Genscript) by batch binding for 2 h at 4°C. The resin was packed into a gravity flow column and washed with a wash buffer containing 20 mM HEPES pH 7.4, 150 mM NaCl, 0.075% (w/v) LMNG, 0.025% (w/v) GDN, and 0.01% (w/v) CHS. Protein elution was achieved by the addition of FLAG-elution buffer (20 mM HEPES pH 7.5, 150 mM NaCl, 0.075% (w/v) LMNG, 0.025% (w/v) GDN, and 0.01% (w/v) CHS and 0.25 mg/mL FLAG peptide). Eluent was then loaded into a pre-washed TALON Metal Affinity Resin (Takara) column and was washed with wash buffer supplemented with 30 mM imidazole. HRV 3C protease was added to the bead slurry and incubated at 4°C for 16h to allow for on-column cleavage. The cleaved sample was collected in wash buffer and concentrated as described above for GPR56.

For the removal of oligomeric fragments, the samples were resolved over a Superose 6 Increase 10/300 GL column (GE Healthcare) with running buffer containing 20 mM HEPES pH 7.5, 150 mM NaCl, 0.00075% (w/v) LMNG, 0.00025% (w/v) GDN and 0.0001% (w/v) CHS. EM fractions containing monomeric receptor were pooled, concentrated and utilized for the cryo-EM experiments. Samples were resolved by SDS-PAGE and immunoblotted utilizing a monoclonal anti-FLAG antibody (THE$^{TM}$ DYKDDDDK Tag Antibody- HRP, mAb, Mouse; GenScript, 1:1000) to confirm the presence of the LPHN3 FLAG-tagged ECR. Further experimental details are provided in Extended Data Figs. 1 and 2.

### *NTF-bound LPHN3 purification and encapsulation in nanodiscs*

Brain polar lipids (BPL, Avanti Polar Lipids, 141101P) were dissolved in chloroform:MeOH (3:2), dried and kept under vacuum overnight. Lipids were hydrated by the addition of 20 mM Hepes, pH 7.5, 150 mM NaCl, 60 mM sodium cholate (30 mM final concentration, assuming molecular weight of 650 gr/mol) and subjected to 10 freeze/thaw cycles with liquid nitrogen. Lipids were sonicated, flash frozen and stored in -80°C until use.

Membrane Scaffold Protein 1D1 (MSP1D1) was prepared as described [40]. In brief, *Escherichia coli* BL21 (DE3) harboring plasmid pET-28a(+) with MSP1D1 was grown overnight at 37°C in Terrific Broth (TB) medium supplemented with 30 μg/mL Kanamycin. Cultures were diluted 1:33

in TB, supplemented with 30 µg/mL Kanamycin, grown at 37°C to 2.3-2.5 $A_{600}$ units, induced by addition of 1 mM IPTG and grown for an additional 3.5 h at 37°C. Cells were harvested, resuspended in MSP lysis buffer (40 mM sodium phosphate, pH 7.4), flash-frozen in liquid nitrogen and stored in -80°C. For MSP1D1 purification, cells were thawed in MSP lysis buffer and supplemented with protease inhibitor (cOmplete mini EDTA-free, Roche) and 1 mM phenylmethanesulfonyl fluoride (PMSF). Cells were sonicated, and the lysate was centrifuged at 30,000 g for 30 min, at 4°C. The supernatant was mixed with Ni-NTA resin (Takara), incubated with agitation for 1 h, at 4°C, packed into a gravity column and the flow-through was discarded. The resin was washed with 4 column volumes (CVs) of MSP wash 1 buffer (40 mM Tris-HCl pH 8.0, 300 mM NaCl), 4 CVs of MSP wash 2 buffer (40 mM Tris-HCl pH 8.0, 300 mM NaCl, 50 mM sodium cholate), 4 CVs of MSP wash 1 buffer and 4 CVs of MSP wash 3 buffer (40 mM Tris-HCl pH 8.0, 300 mM NaCl, 30 mM imidazole). The protein was eluted with MSP elution buffer (40 mM Tris-HCl pH 8.0, 300 mM NaCl, 300 mM imidazole). The eluted protein was concentrated to ~20 mg/mL using a 10 kDa concentrator (Amicon Ultra Centrifugal Filter MWCO 10 kDa, Merck-Millipore) and dialyzed at 4°C against buffer containing 20 mM Hepes, pH 7.5, 150 mM NaCl.

pMSP1D1 was a gift from Stephen Sligar (Addgene plasmid #20061; http://n2t.net/addgene:20061 ; RRID:Addgene_20061) [41].

The expression of LPHN3 and membrane preparation were performed in a similar manner to the detergent-based purification schemes described above with some exceptions. Membranes were homogenized in 1% (w/v) n-Dodecyl-β-D-Maltopyranoside (DDM, Anatrace) instead of LMNG and the affinity purification steps were performed in a buffer containing 0.1% (w/v) DDM and 0.01% (w/v) CHS. Protein was concentrated to ~150 µM using a 100 kDa concentrator and reconstituted into MSP1D1 using the following molar ratios: LPHN3 : 7H-MSP1D1 – 1 : 3 ; 7H-MSP1D1 : BPL Lipids – 1:70, in the presence of 33.8 mM sodium cholate, and 3.7% v/v glycerol. The mixture was incubated in the dark, for 1 h at 4°C with gentle stirring, followed by the addition of Bio-Beads SM-2 Resin (Bio-Rad) (1 gr / 1 mL mixture) and an incubation for an additional 1 h at 4°C. Bio-Beads were then added and incubated for 16 h at 4°C. Bio-Beads were removed by centrifugation, and the mixture was incubated with Anti-DYKDDDDK G1 Affinity Resin (Genscript) for 1 h, at 4°C. The resin was packed into a gravity flow column and washed with FLAG Wash Buffer (20 mM Hepes, pH 7.5, 150 mM NaCl, 10% v/v glycerol). The protein was eluted with FLAG Elution Buffer (20 mM Hepes, pH 7.5, 150 mM NaCl, 10% v/v glycerol, 0.25 mg/mL FLAG peptide). Eluted nanodiscs were then incubated with Ni-NTA resin for 1 h, at 4°C with gentle stirring. The resin was packed into a gravity column, washed with nanodisc Ni-NTA Wash Buffer (20 mM Hepes, pH 7.5, 150 mM NaCl, 10% v/v glycerol, 10 mM imidazole) and eluted with nanodisc Ni-NTA Elution Buffer (20 mM Hepes, pH 7.5, 150 mM NaCl, 10% v/v glycerol, 250 mM imidazole). The sample was concentrated to ~500 µl using a 100 kDa protein concentrator and loaded onto Superose 6 Increase 10/300 GL column that was resolved using size exclusion chromatography (SEC) buffer (20 mM Hepes, pH 7.5, 150 mM NaCl). Fractions were analyzed by fluorescence (Em: 295 nm, Ex: 330 nm) and by SDS-PAGE. Fractions containing both the N- and C- termini of LPHN3 and MSP1D1 were combined, concentrated and utilized for the cryo-EM studies.

*Expression and purification of active-state receptor complexes*

*Sf*9 cells were co-infected with 7TM-GPR56 or 7TM-LPHN3 and miniG$_{13/i15}$ dual baculoviruses and incubated for 48 h at 27 ºC. Cells were harvested by centrifugation and resuspended by Dounce homogenization in buffer containing 20 mM Hepes pH 7.5, 100 mM NaCl, 10 mM $MgCl_2$, 10% v/v glycerol, 0.1 mM tris(2-carboxyethyl) phosphine (TCEP), protease inhibitors cocktail (20 µM leupeptin, 5.2 µg/mL aprotinin, 1.4µg/mL pepstatin, 0.023 mg/mL PMSF and 1 mM benzamidine) and benzonase nuclease (Millipore). Following the addition of 25 mU/mL apyrase (Sigma), the cell suspension was incubated at room temperature for 2 h with gentle stirring. Detergent was added to reach a 1% (w/v) concentration (0.8% lauryl maltose neopentyl glycol (LMNG, Anatrace), 0.2% (w/v) glycol-diosgenin (GDN, Sigma Aldrich), 0.1% (w/v) cholesteryl hemisuccinate (CHS, Anatrace)), and incubated for 1.5 h at 4 ºC. Solubilized proteins were clarified by centrifugation at 40,000 g for 30 min at 4 ºC and the supernatant was batch bound to pre-washed HisPur Ni-NTA affinity resin (Thermo Scientific) in the presence of 30 mM imidazole for 1 h at 4 ºC with gentle stirring. Beads were packed into a gravity column and washed with Ni-NTA buffer (20 mM HEPES pH: 7.5, 100 mM NaCl, 2 mM $MgCl_2$, 30 mM imidazole, 20% v/v Glycerol, 20 µM leupeptin, 1 mM benzamidine, 0.1 mM TCEP, while slowly decreasing the detergent concentration of the wash to 0.01% (w/v) (0.008% (w/v) LMNG, 0.002% (w/v) GDN, 0.001% (w/v) CHS). Protein was eluted using the final wash buffer containing 250 mM imidazole and concentrated to ~200 µL. The concentrated eluate was incubated O/N with 1 mg of HRV-3C protease (Sigma-Aldrich) per 50 mg of protein. Following 3C digestion, the sample was resolved over an Enrich SEC 650 column (Bio-Rad) using SEC running buffer containing 20 mM HEPES: pH 7.5, 100 mM NaCl, 2 mM $MgCl_2$, 0.1 mM TCEP and 0.001% (w/v) detergent mix. Fractions corresponding to receptors with complexed G protein were pooled and concentrated for the preparation of cryo-EM grids.

### Cryo-EM data acquisition and processing for the NTF-bound LPHN3 in detergents and nanodiscs

3.5 µL of purified samples at 8-10 mg/mL were applied on glow-discharged (90 sec, 15 mA, PELCO easiGlow™, TED PELLA Inc.) holey carbon gold grids (Quantifoil R1.2/1.3, 200 mesh). The grids were blotted using a Vitrobot Mark IV (FEI) with 3 s blotting time at 22°C in 100% humidity, and plunge-frozen in liquid ethane. A total of 10,870 movies were recorded on a Titan Krios electron microscope (ThermoFisher Scientific - FEI) operating at 300 kV at a magnification of x105K and corresponding to a magnified pixel size of 0.86 Å. A BioQuantum energy filter (Gatan) was operated with an energy slit width of 20 eV. Micrographs were recorded using a K3 direct electron camera (Gatan) with an exposure rate of ∼30.6 electrons/Å$^2$/s and defocus values ranging from −0.8 μm to −2.3 μm. The total exposure time was 1.49 s, and intermediate frames were recorded in 0.033 s intervals resulting in an accumulated dose of ~45.5 electrons per Å$^2$ and a total of 45 frames per micrograph. Automatic data acquisition was done using EPU (ThermoFisher Scientific - FEI). For the nanodisc sample, the micrographs were recorded using a Falcon 3 direct electron detector (FEI, ThermoFisher Scientific) with an exposure rate of ~1.17 electrons/Å$^2$/s and defocus values ranging from −0.8 μm to −2.3 μm. The total exposure time was 35 s, and intermediate frames were recorded in 0.875 s intervals resulting in an accumulated dose of ~41 electrons per Å$^2$ and a total of 40 frames per micrograph. A total of 3053 micrographs were collected. Micrographs were subjected to beam-induced motion correction using RELION 3.1 MotionCor2 [42]. CTF parameters for each micrograph were determined by CTFFIND4 [43]. Initial particle selection in RELION 3.1 [42] was done manually followed by particle extraction and 2D classification for a template guided particle picking that resulted in an initial set of 6,246,443 particle projections (32,494 for the nanodisc data). The particles were subjected to reference-free two-dimensional classifications and three-dimensional (3D) classifications in RELION 3.1 [42]. An *ab-inito* model low pass filtered to 40 Å was used as an initial reference model for maximum-likelihood-based 3D classifications. A total of 187,766 particles were subjected to 3D refinement and contributed to the map presented in Fig. 1c. A flowchart describing data processing steps is in Extended Data Fig. 1.

### Cryo-EM data acquisition and processing for FL-GPR56 and the active state complexes of GPR56 and LPHN3

3 μl of purified samples at concentrations of 5 mg/mL, 7.5 mg/mL or 4.5 mg/mL of the FL-GPR56, GPR56/miniG$_{13/i}$ or LPHN3/miniG$_{13/i}$ complexes, respectively, were applied to glow-discharged (50 seconds at 10 mA) UltrAuFoil gold grids (Quantifoil, Au300-R1.2/1.3) in 100% humidity at 4°C. Samples were blotted for 1 second and plunged-frozen in liquid ethane using a Vitrobot Mark IV (Thermo Fisher Scientific). Cryo-EM imaging was performed on Titan Krios

(ThermoFisher) electron microscopes operated at 300 kV with a K3 Summit direct electron detector (Gatan) at a magnification of 55,000 X (0.8677 Å/pixel) for GPR56/miniG$_{13/i}$ complex and 57,050 X (0.8521 Å/pixel) for the FL-GPR56 and LPHN3/miniG$_{13/i}$ complex in counting mode. For FL-GPR56 4,718 movies, dose fractioned over 79 frames, were recorded for 0.0255 sec/frame for a total dose of 65.25 electrons/Å$^2$ in super-resolution mode with a defocus range of 0.6-1.4 µm. For the GPR56/miniG$_{13/i}$ complex, 6,653 movies, dose fractioned over 57 frames, were recorded for 0.05 sec/frame for a total dose of 60.79 electrons/Å$^2$ in super-resolution mode with a defocus range of 0.8-1.8 µm. For the LPHN3/miniG$_{13/i}$ complex, 4,667 movies, dose fractioned over 63 frames, were recorded for 0.04 sec/frame for a total dose of 68.95 electrons/Å$^2$ in super-resolution mode with a defocus range of 0.6-1.8 µm using SerialEM [44]. Cryo-EM data processing was performed with cryoSPARC [45]. For FL-GPR56, an initial set 2,318,547 particles were selected and subjected to 2D and 3D classification with a total of 13,965 particles contributing to the map presented in Fig. 1d. A total of 6,794,073 particles were extracted from the corrected 6,653 micrographs for the GPR56/miniG$_{13/i}$ complex. Multiple 2D and 3D classification rounds were performed. A subset of 541,279 particles were subjected to homogeneous refinement followed by local refinements of the active GPR56 transmembrane domain and G protein with resolutions at 2.7 Å and 2.9 Å, respectively. A total of 4,242,031 particles were extracted from the corrected 4,667 micrographs for the LPHN3/miniG$_{13/i}$ complex. After 2D and 3D classification, a subset of 440,914 particles were subjected to homogeneous and non-uniform refinements followed by local refinements of the active LPHN3 transmembrane domain and G protein with resolutions at 2.9 Å and 3.1 Å, respectively. Maps resulting from the local refinements were sharpened using DeepEMhancer (https://doi.org/10.1101/2020.06.12.148296) and combined in Chimera [46] contributing to the maps presented in Fig. 1f-g. Flowcharts describing data processing steps are presented in the Extended Data Figs. 2d, 4 and 5.

### Model building and refinement for active complexes

Homology models prepared with Phyre2 [47] for the 7TM domains of LPHN3 and GPR56, the Ras domain of $G_{\alpha13}$ (PDB ID: 1ZCB [48]), and coordinates for $G_{\beta1}$ and $G_{\gamma2}$ subunits (PDB ID: 7MTS [49]) to build the mini$G_{\alpha13/i}$, were used as initial models for docking into the EM density maps using Chimera [46]. The models were subjected to iterative rounds of manual refinement in Coot [50] and real-space refinement in Phenix [51]. Validation of cryo-EM maps and models was performed with Phenix [51] comprehensive cryo-EM validation. Model statistics were validated with Molprobity [52]. Final refinement statistics are provided in Extended Data Table 1. UCSF Chimera [46] and ChimeraX [53] were used for map/model visualizations and figure preparation.

### Molecular dynamics simulations for LPHN3 and analysis

Starting from our cryo-EM structure of LPHN3-mini$G_{13}$ complex, the G protein was removed, and the receptor alone was oriented in a lipid bilayer with the OPM webserver [54]. PDB files were prepared both with and without the first 7 N-terminal residues of the tethered agonist sequence. The CHARMM-GUI [55] was used to prepare the system in a 1-palmitoyl-2-oleoyl-sn-glycero-3-phosphocholine POPC/CHS lipid bilayer solvated in TIP3P water [56] with 150 mM NaCl. Input files were generated with the CHARMM36m forcefield (CHARMM36m) with hydrogen mass repartitioning. Simulations were run in the NAMD2.14 [57] software using a Langevin thermostat and a Nosé-Hoover Langevin piston barostat at 1 atm with a period of 50 fs and decay of 25 fs. Nonbonded interactions were smoothed starting at 10 Å to 12 Å with long-range interactions treated with particle mesh Ewald (PME) and periodic boundary conditions were employed. The system was restrained with 5 kcal/mol/Å$^2$ harmonic restraints on all non-water, non-ion, and non-hydrogen atoms, minimized for 1500 steps, and gradually heated from 0 to 303.15 K in increments of 20 K simulating for 0.4 ns at each increment. An additional 10 ns of equilibration was run before restraints were removed from lipid atoms for an additional 10 ns of equilibration. 5 kcal/mol/Å$^2$ harmonic restraints were then applied to only protein CA atoms for 10 ns increments while the force constant of the restraints was gradually reduced to 2.5, 1.0, and 0.5 kcal/mol/Å$^2$. The first 30 ns of unrestrained simulation was also discarded as equilibration and 1 μs of MD simulations were run using a 4 fs timestep with SHAKE and SETTLE [58,59]. For simulations of the tethered agonist peptide alone, setup and simulation were almost identical, except for the absence of a lipid bilayer, the lack of harmonic restraints used during equilibration, and the fact that three replicates were performed as that was sufficient for convergence of the calculated quantities. Pymol (https://pymol.org/2/) was used for visualization of MD simulations experiment results.

**Preparation and Quantification of aGPCR membrane homogenates.**

Wild type or alanine substituted GPR56 or LPHN3 mutant receptors (achieved through site-directed mutagenesis) were expressed in 50 mL *Sf*9 cultures through baculoviruses infection. Cells were harvested 48 h post infection and lysed by nitrogen cavitation in a lysis buffer containing 20 mM Hepes pH 7.4, 1 mM EGTA, and protease inhibitor cocktail (23 µg/mL phenylmethylsulfonyl fluoride, 21 ug/mL L-1-p-tosylamino-2-phenylethyl-chloromethyl ketone, 21 µg/mL Na-p-tosyl-L-lysine-chloromethyl ketone, 3.3 µg/mL leupeptin and 3.3 µg/mL soy bean trypsin inhibitor). Cell debris was cleared by centrifugation at 1000 g and membranes were precipitated at 100,000 g. The membranes were Dounce homogenized in lysis buffer, collected at 100,000 g, and homogenized in lysis buffer supplemented with 12% w/v sucrose. Total protein content of membrane homogenates was measured by Bradford assay and samples containing ~5-10 mg total protein were stored at -80ºC. For western blotting, 10 µg of 7TM/CTF membranes were resolved by SDS-PAGE and transferred to polyvinylidene difluoride (PVDF) membranes. Membranes were blocked in 5% w/v bovine serum albumin (BSA) in PBS for 30 min, and incubated at 4 ºC overnight with 0.1 µg/mL pentaHis antibody (Qiagen). Membranes were washed with TBST, incubated with 1:5000 IR-800 donkey anti-mouse antibody (LiCor) in

BLOTTO (TBS with 5% w/v milk and 0.1% NP-40) for 1 hr at 22 ºC. After incubation, membranes were washed twice in TBST, twice in TBS, and imaged using an Invitrogen iBright system. For full-length GPR56 membranes, blots were blocked in BLOTTO and probed using antibodies specific for the NTF (R&D Systems, Cat. No. AF4634) and the CTF (EMD Millipore, Cat. No. ABS1028) and processed with 1:5000 IR-800 donkey anti-rabbit antibody (LiCor) or 1:5000 Alexa-Fluor 647 donkey anti-sheep antibody (ThermoFisher Scientific) as described above. Triplicate western blot lanes were quantified via pixel densitometry using Adobe Photoshop, and relative receptor levels were plotted using GraphPad Prism version 9.0.2 (GraphPad Prism) for Windows, GraphPad Software, San Diego, California USA, www.graphpad.com (Extended Data Fig. 7, Supplementary Table 1 and Supplementary Figure 1).

### [$^{35}$S]-GTPγS Binding Activity Assays

Membrane homogenates (5 µg / assay time point) were reconstituted with 200 nM purified $G\alpha_{13}$ and 500 nM purified $G\beta_1G\gamma_2$ in binding buffer containing 50 mM Hepes pH 7.4, 1 mM dithiothreitol (DTT), 1 mM EDTA, and 3 µg/mL purified BSA (NEB). Heterotrimeric $G_{13}$ proteins (wild type $G_{13}$, $G_{13/i15}$, $G_{13/i29}$) were expressed in *Trichoplusia ni* (High-Five™) insect cells and purified as described [60].

Kinetic GTPγS binding assays were initiated by the addition of an equal volume of binding buffer containing 50 mM NaCl, 10 mM $MgCl_2$, 20 µM GDP, 4 µM [$^{35}$S]-GTPγS (25-50,000 cpm / pmol). Endpoint assays or aliquots withdrawn from kinetic assays were quenched with 20 mM Tris pH 7.7, 100 mM NaCl, 10 mM $MgCl_2$, 1 mM GTP, 0.08% w/v lubrol C12E10 and filtered through Whatman GF/C filters using a Brandel Harvester. The filters were washed, dried, and subjected to liquid scintillation counting.

Testing of G protein partners for the structural studies was carried out similarly, with the following exceptions: membrane homogenates (5 µg) were reconstituted with 250 nM purified $G\alpha_{13}\beta_1\gamma_2$, $G\alpha_{13i15}\beta_1\gamma_2$, or $G\alpha_{13i29}\beta_1\gamma_2$ heterotrimer in binding buffer with 20 µM GDP, then pre-incubated for 10 min at 25 °C. The assay was initiated by the addition of an equal volume of binding buffer supplemented with 50 mM NaCl, 10 mM $MgCl_2$, 20 µM GDP, and 4 µM [$^{35}$S]-GTPγS (25-50,000 cpm/pmol). Following a 10 min incubation at 25ºC, reactions were quenched and filtered through Protran BA85 nitrocellulose filters (GE Healthcare) using a Millipore vacuum manifold. Filters were then processed as described above. Data analysis and representation was performed using GraphPad Prism.

**Measurement of aGPCR relative cell surface levels**

Log phase 10 ml *Sf*9 cultures were infected with 1/100 volume of amplified aGPCR virus for 36 h. Cells were washed twice at 4 ºC with PBS and protease inhibitor cocktail prior to incubation with 2 mM Sulfo-NHS-LC-Biotin (ThermoFisher) in PBS for 15 min at 22 ºC. Cells were quenched and washed twice with TBS and lysed at 4 ºC for 30 min in lysis buffer (25 mM Hepes pH 7.4, 150 mM NaCl, 2 mM $MgCl_2$, 1 mM EDTA, 1% w/v Triton X-100, 2% v/v glycerol, protease inhibitor cocktail). Lysates were clarified by centrifugation at 21,000 g, incubation with a 50 µl bed volume of G25 Sephadex and reclarification at 21,000 g. The supernatant was tumbled at 4 ºC for 1 h with a 40 µl bed volume of Streptavidin Sepharose HP (Cytiva). The resin was washed two times with lysis buffer and eluted with reducing SDS-PAGE sample buffer at 42 ºC for 5 min. AGPCRs were resolved by SDS-PAGE, immunoblotted with the pentaHis antibody (Qiagen).

**References**

39 Kim, K. *et al.* Structure of a Hallucinogen-Activated Gq-Coupled 5-HT<sub>2A</sub> Serotonin Receptor. *Cell* **182**, 1574-1588.e1519, doi:10.1016/j.cell.2020.08.024 (2020).

40 Bayburt, T. H., Grinkova, Y. V. & Sligar, S. G. Self-Assembly of Discoidal Phospholipid Bilayer Nanoparticles with Membrane Scaffold Proteins. *Nano Letters* **2**, 853-856, doi:10.1021/nl025623k (2002).

41 Denisov, I. G., Grinkova, Y. V., Lazarides, A. A. & Sligar, S. G. Directed Self-Assembly of Monodisperse Phospholipid Bilayer Nanodiscs with Controlled Size. *Journal of the American Chemical Society* **126**, 3477-3487, doi:10.1021/ja0393574 (2004).

42 Zivanov, J. *et al.* New tools for automated high-resolution cryo-EM structure determination in RELION-3. *eLife* **7**, e42166, doi:10.7554/eLife.42166 (2018).

43 Rohou, A. & Grigorieff, N. CTFFIND4: Fast and accurate defocus estimation from electron micrographs. *J Struct Biol* **192**, 216-221, doi:10.1016/j.jsb.2015.08.008 (2015).

44 Mastronarde, D. N. Automated electron microscope tomography using robust prediction of specimen movements. *J Struct Biol* **152**, 36-51, doi:10.1016/j.jsb.2005.07.007 (2005).

45 Punjani, A., Rubinstein, J. L., Fleet, D. J. & Brubaker, M. A. cryoSPARC: algorithms for rapid unsupervised cryo-EM structure determination. *Nat Methods* **14**, 290-296, doi:10.1038/nmeth.4169 (2017).

46 Pettersen, E. F. *et al.* UCSF Chimera--a visualization system for exploratory research and analysis. *J Comput Chem* **25**, 1605-1612, doi:10.1002/jcc.20084 (2004).

47 Kelley, L. A., Mezulis, S., Yates, C. M., Wass, M. N. & Sternberg, M. J. E. The Phyre2 web portal for protein modeling, prediction and analysis. *Nature Protocols* **10**, 845-858, doi:10.1038/nprot.2015.053 (2015).

48 Kreutz, B. *et al.* A new approach to producing functional G alpha subunits yields the activated and deactivated structures of G alpha(12/13) proteins. *Biochemistry* **45**, 167-174, doi:10.1021/bi051729t (2006).

49 Seven, A. B. *et al.* G-protein activation by a metabotropic glutamate receptor. *Nature* **595**, 450-454, doi:10.1038/s41586-021-03680-3 (2021).

50 Emsley, P., Lohkamp, B., Scott, W. G. & Cowtan, K. Features and development of Coot. *Acta Crystallogr D Biol Crystallogr* **66**, 486-501, doi:10.1107/s0907444910007493 (2010).

51 Liebschner, D. *et al.* Macromolecular structure determination using X-rays, neutrons and electrons: recent developments in Phenix. *Acta Crystallogr D Struct Biol* **75**, 861-877, doi:10.1107/s2059798319011471 (2019).

52 Chen, V. B. *et al.* MolProbity: all-atom structure validation for macromolecular crystallography. *Acta Crystallogr D Biol Crystallogr* **66**, 12-21, doi:10.1107/s0907444909042073 (2010).

53 Pettersen, E. F. *et al.* UCSF ChimeraX: Structure visualization for researchers, educators, and developers. *Protein Sci* **30**, 70-82, doi:10.1002/pro.3943 (2021).

54 Lomize, M. A., Pogozheva, I. D., Joo, H., Mosberg, H. I. & Lomize, A. L. OPM database and PPM web server: resources for positioning of proteins in membranes. *Nucleic Acids Research* **40**, D370-D376, doi:10.1093/nar/gkr703 (2011).

55 Lee, J. *et al.* CHARMM-GUI Input Generator for NAMD, Gromacs, Amber, Openmm, and CHARMM/OpenMM Simulations using the CHARMM36 Additive Force Field. *Biophysical Journal* **110**, 641a, doi:10.1016/j.bpj.2015.11.3431 (2016).

56 Jorgensen, W. L., Chandrasekhar, J., Madura, J. D., Impey, R. W. & Klein, M. L. Comparison of simple potential functions for simulating liquid water. *The Journal of Chemical Physics* **79**, 926-935, doi:10.1063/1.445869 (1983).

57 Phillips, J. C. *et al.* Scalable molecular dynamics with NAMD. *Journal of Computational Chemistry* **26**, 1781-1802, doi:https://doi.org/10.1002/jcc.20289 (2005).

58 Ryckaert, J.-P., Ciccotti, G. & Berendsen, H. J. C. Numerical integration of the cartesian equations of motion of a system with constraints: molecular dynamics of n-alkanes. *Journal of Computational Physics* **23**, 327-341, doi:https://doi.org/10.1016/0021-9991(77)90098-5 (1977).

59 Miyamoto, S. & Kollman, P. A. Settle: An analytical version of the SHAKE and RATTLE algorithm for rigid water models. *Journal of Computational Chemistry* **13**, 952-962, doi:https://doi.org/10.1002/jcc.540130805 (1992).

60 Dror, R. O. *et al.* Structural basis for nucleotide exchange in heterotrimeric G proteins. *Science* **348**, 1361-1365, doi:doi:10.1126/science.aaa5264 (2015).

## Acknowledgments

We thank Elizabeth Montabana at the Stanford cEMc facility and Dr. Nadav Elad at the Weizmann Institute of Science microscopy unit for support with data collection. This work was supported by the Mathers Foundation (MF-1804-00129) (G. S.), the European Research Council (ERC) under the European Union's Horizon 2020 research and innovation programme (No. 949364) and the Minerva Foundation (M. S. -B) and R01s GM120110 and NS103946 (G.G.T.). E.H.Y is the recipient of the IASH Fellowships for Israeli Postdoctoral Fellows. A.V. is supported by NHLBI F31-HL152563.

## Author contributions

X.B.-A. and G.G.T. designed GPR56 and G protein constructs. D.M., M. S.-B and G.G.T. designed LPHN3 constructs. X.B.-A. expressed and purified active GPR56 and LPHN3 receptors, G proteins and complexes, prepared cryo-EM grids, oversaw data collection, processed cryo-EM data for complexes, modeled the structures, analyzed the structural data and prepared the manuscript. R. M. N. performed mutagenesis experiments, cloned G protein constructs, purified G proteins, assisted in the purification of complexes, analyzed data and prepared the manuscript. A.L.V. and H.S. conducted G protein activation experiments. D.M. expressed and purified NTF-bound LPHN3 receptors, prepared cryo-EM grids, collected and processed cryo-EM data and assisted in figure preparation. F. H. purified and processed cryo-EM data for FL-GPR56. O. P. prepared cryo-EM grids, performed data collection. M.M.P.-S. performed G protein activity assays and assisted in figure preparation. M. J. R. performed and analyzed molecular dynamic simulations. E.H.Y. Purified LPHN3 and reconstituted in nanodiscs. A. B. S. assisted in cryo-EM data processing. M. C. P. assisted in protein purifications and mutagenesis. J. G. M. assisted in biochemical assays and cloning. A.L.V. F.K., and G.G.T. purified G proteins and prepared aGPCR membranes.  X. B.-A., R. M. N., M. S.-B, G. G. T. and G. S. wrote the manuscript. G. S. supervised the project.

## Competing interests

The authors declare no competing interests.

## Data availability

All data generated or analyzed in this study are included in this article and the Supplementary Information. The cryo-EM density maps and corresponding coordinates have been deposited in the Electron Microscopy Data Bank (EMDB) and the Protein Data Bank (PDB), respectively, under the following accession codes: EMD-25077 and 7SF8 (7TM GPR56-miniG$_{13}$) and EMD-25076 and 7SF7 (7TM LPHN3-miniG$_{13}$).

## Extended Data Figure Legends

**Extended Data Figure 1. a,** Design for the NTF-bound LPHN3 construct used for structural studies. Human LPHN3 (V1, residues 495-1138) was cloned into pFastBac containing a hemagglutinin signal peptide tag (HA) and a cleavable N-terminal FLAG-tag. The construct included a C-terminal cleavable GFP followed by a His$_6$ tag. **b,** Size exclusion chromatography (SEC) profile of LPHN3. Samples corresponding to the main monomeric (grey) fractions were combined and used for cryo-EM studies. **c,** Coomassie stained SDS-PAGE of the pooled protein sample visualized by cryo-EM showing the presence of the N-terminal ECR and the 7TM domain. **d,** Anti-FLAG Western-blot analysis of the LPHN3 sample purified in detergent. **e,** Cryo-EM reference-free 2D class averages of LPHN3 purified in detergent and **f,** processing flow chart of the NTF-bound LPHN3 sample, including particle selection, 2D and 3D classifications. **g,** Size exclusion chromatography (SEC) of LPHN3 embedded in lipid nanodiscs composed of MSP1D1 and brain polar lipids (BPL). Yellow bars indicate fluorescence of lipids (Ex: 295 nm, Em: 330 nm). Arrowed bars indicate signal overload. Grey shaded area shows fractions that were used for the cryo-EM analysis. **h,** SDS-PAGE stained with InstantBlue, showing purified MSP1D1, purified LPHN3 in DDM, reconstituted LPHN3 in lipid nanodiscs before SEC, and selected SEC fractions of the nanodiscs. Bold fractions were used for cryo-EM. **i,** Representative reference free 2D class averages of LPHN3 embedded in lipid nanodiscs.

**Extended Data Figure 2. a,** Design for the full-length cleavage deficient (CD, H381S) GPR56 construct used for structural studies. Human GPR56 (V2-FL) was cloned into pFastBac containing a hemagglutinin signal peptide tag (HA) and a cleavable N-terminal FLAG-tag. The construct included a C-terminal cleavable $His_6$ tag. **b,** Size exclusion chromatography (SEC) profile of full-length GPR56. Fractions corresponding to the monomeric peak (grey) were collected and used for structural studies. **c,** Coomassie stained SDS-PAGE of the FL-GPR56 sample used for cryo-EM analysis. **d,** Cryo-EM data processing workflow of the FL-GPR56 sample. **e, f.** Low resolution 3D maps of NTF-bound receptor conformations with docked structures of the ECR of **e,** GPR56 and **f,** LPHN3. The GAIN domains and TA peptides are colored in blue and cyan for GPR56 and in magenta and light pink for LPHN3. Domains are labeled. Docked available ECR crystal structures corresponding to PDB 5KVM and 4DLQ for GPR56 and LPHN1, respectively. Scale bars are provided in the left bottom corner.

**Extended Data Figure 3. a,** Design for the tethered agonist complex constructs used in the study. Receptors are presented on top, where sequences corresponding to the TA and 7TM regions of GPR56 and LPHN3 were inserted after a hemagglutinin signal peptide (HA) and a methionine residue. Expression vector for the $miniG_{13}$ heterotrimer presented at the bottom. **b,** The $MiniG_{\alpha13/i15}$ sequence. Residues at the N-terminus corresponding to $G_{\alpha i2}$ sequence are in grey. The linker replacing the alpha helical domain is in yellow. Residues corresponding to the stabilizing mutations $G57D^{S1H1.03}$, $E58N^{S1H1.04}$, $S248D^{S4.07}$, $E251D^{S4H3.03}$, $I271D^{H3.08}$, $I355A^{H5.04}$, $V358I^{H5.07}$ are underlined and presented in bold. **c,** Size-exclusion chromatography (SEC) profiles of purified $miniG_{13}$-coupled GPR56 (left) and -LPHN3 (right) with insets showing Coomassie-stained SDS-PAGE of the SEC complex peaks.

**Extended Data Figure 4. a,** Workflow of cryo-EM data processing for the active tethered agonist bound 7TM-GPR56/miniG$_{13}$ complex. **b,** Angular distribution heat map of particle projections for 7TM-GPR56/miniG$_{13}$ reconstruction. **c,** Gold standard Fourier shell correlation (FSC) curve for receptor and miniG$_{13}$ reconstructions. Dashed line represents the overall nominal resolution of each reconstruction at 0.143 FSC calculated by CryoSPARC. **d,** Overall composite cryo-EM map for the 7TM-GPR56/miniG$_{13}$ complex with chain assignments for its components. **e,** Cryo-EM density for TMs 1-7, the α5 helix of miniGα$_{13/i}$ and the bound tethered agonist for the 7TM-GPR56/miniG$_{13}$ complex.

**Extended Data Figure 5. a,** Workflow of cryo-EM data processing for the active tethered agonist bound 7TM-LPHN3/miniG$_{13}$ complex. **b,** Angular distribution heat map of particles for 7TM-LPHN3/miniG$_{13}$ reconstruction. **c,** Gold standard Fourier shell correlation (FSC) curve for receptor and miniG$_{13}$ reconstructions. Dashed line represents the overall nominal resolution of each reconstruction at 0.143 FSC calculated by CryoSPARC. **d,** Overall composite cryo-EM map for the 7TM-LPHN3/miniG$_{13}$ complex with chain assignments for its components. **e,** Cryo-EM density for TMs 1-7, the α5 helix of miniGα$_{13/i}$ and the bound tethered agonist for the 7TM-LPHN3/miniG$_{13}$ complex.

**Extended Data Figure 6.** Kinetic measurements of receptor-stimulated G protein 13 [$^{35}$S]-GTPγS binding in membranes normalized to the activities of wild type (WT) GPR56 or LPHN3. 7TM/CTF-only truncated receptors with **a, b***,* point mutations at the TA residues. **c, d,** TA-interacting point mutants. **e, f,** G protein interaction site point mutants. **g, h,** 7TM core-stabilizing point mutants. Note: GPR56 Q644A and LPHN3 E948A were found at low abundance, thus potentially explaining their reduced activities. **i,** Equivalent amounts of WT, W617$^{6.53}$A, F637$^{7.42}$A, and F454$^{2.64}$A full-length GPR56 holoreceptors were activated by ice-cold urea treatment to dissociate NTFs from CTFs prior to measurement of G13 initial GTPγS binding rates at 20 ºC. The urea-dependent changes in approximated initial linear rates demonstrate that wild type GPR56 was activated by urea significantly more than each mutant, indicating that the mutations impart reduced functional activity and that the mutant receptors are not completely dysfunctional or mis-folded. Data represent the average of each kinetic reaction measured as technical triplicates with error bars representing +/- S.D. Unpaired, two-tailed student's t tests were used to determine significance between initial rates. * = $p < 0.05$, **** = $p < 0.0001$. Further detailed statistical information can be found in Supplementary Data Table 1. **j,** Relative aGPCR cell surface levels for selected mutants and WT receptors were measured by intact cell biotinylation, streptavidin pulldown and anti-His tag immunoblotting.

**Extended Data Figure 7. a,** Relative abundances of CTF-only truncated GPR56 receptors in membrane homogenates determined by immunoblotting for anti-His tag. **b,** Relative abundances of CTF-only truncated LPHN3 receptors in membrane homogenates determined by immunoblotting for anti-His tag. **c,** Relative abundances of holoreceptor GPR56 NTFs and CTFs before and after treatment of membrane homogenates with ice-cold 6M urea. CTF was immunoblotted for via a GPR56-specific CTF antibody, and NTF was immunoblotted for via a GPR56-specific NTF antibody. *Multiple glycosylated NTF bands. Data represent the mean band intensity of western blots performed in triplicate with error bars representing +/- S.D. Unpaired, two-tailed student's *t* tests were used to determine significance between wild type and mutant receptors with reduced abundances. * = $p < 0.05$. Further detailed statistical information can be found in Supplementary Data Table 1.

**Extended Data Figure 8. a, b,** Density corresponding to the TA peptide and ECL2 in GPR56 (a) and LPHN3 (b), indicating that the TA and loop are penetrating the 7TM cavity. **c, d,** Residues surrounding the toggle switch residue ($W^{6.53}$) in GPR56 (**c**) and LPHN3 (**d**)**.** Electrostatic interactions are shown as dotted grey lines. **e,** Superposition of GPR56 and

LPHN3, showing similarities in 7TM domain conformation. **f,** $G_{13}$ GTPγS binding activity for mutants LPHN3 (magenta) and GPR56 (blue) that interact with $W^{6.53}$. Data represent mean of biologically independent reactions performed in triplicate with error bars representing +/- S.D. RM one-way ANOVA was used to determine significance between mutants and WT. Further detailed statistical information can be found in Supplementary Data Table 1.

**Extended Data Figure 9. Molecular dynamics simulations for the LPHN3 tethered agonist and its binding to the 7TM domain. a,** Four snapshots of the LPHN3 TA peptide MD simulations in solution spaced 200 ns apart. **b,** Average secondary structure percentages of LPHN3 peptide from MD simulations. '$\alpha$' refers to the very broad range of $-160 \leq \varphi \leq -20$; $-120 \leq \psi \leq 50$; 'β', beta-sheet; 'PP2', polyproline 2. **c, d,** Cryo-EM structure of LPHN3 colored by the difference in RMSF values between wild-type MD simulations and simulations with the tethered agonist (TA) region (dark gray) removed. Positive values indicate an increase in flexibility when the TA is deleted. **a** and **b** correspond to two different color scales.

**Extended Data Figure 10. a-b,** Overall structural comparison of 7TM domains of G protein coupled GPR56 (blue) with active state Family B1 receptors: GLP1R (PDB ID: 5VAI; receptor in brown, GLP1 peptide in tan), GCGR (PDB ID: 6WPW; receptor in dark green, glucagon derivative ZP3780 in light green) and calcitonin receptor (PDB ID: 5UZ7; orange). **a,** side view showing similarities in 7TM domain topology and **b,** top view with superposition of B1 agonists with GPR56 TA in the orthosteric site. **c,** Superposition of glucocorticoid ligand-bound GPR97 (PDB ID: 7D77, light grey) with GPR56 (blue) and LPHN3 (magenta). Arrows are indicating differences in TM1, TM6 and TM7 between the ligand and to TA-bound structures. **d,** Top view of superimposed GPR56 and LPHN3 complexes showing positioning of mini-$G_{13}$ N-terminal helix (αN) with respect to the receptor TMs. **e,** Superposition of GPR56 bound mini-$G_{\alpha 13}$ (gold) vs. 5HT1A (PDB ID: 6G79) bound mini-$G_{\alpha o}$ (green). **f,** GTPγS binding assay for recombinant $G_{13}$

proteins in which the authentic N-terminus of $G_{\alpha 13}$ was replaced with 15 or 29 residues of the $G_{\alpha i2}$ αN to improve expression, stability and ability to interact with receptor. Stimulation of $G_{13/i29}$ nucleotide exchange by both receptors GPR56 (blue) and LPHN3 (magenta) was reduced substantially when compared to wild type $G_{13}$ or $G_{13/i15}$. Receptor constructs used in this assay are the TA-decrypted GPR56 and LPHN3. Data displayed as mean of reactions (n=18 for all except GPR56 + $G_{13/i29}$, n=17, and LPHN3 + $G_{13/i29}$, n=16) with error bars representing +/- S.E.M. Statistical significance between experimental condition and corresponding control group was calculated using Mann-Whitney analysis, n.s. = not significant, **** = $p < 0.0001$. Further detailed statistical information, including exact p values, can be found in Supplementary Data Table 1. **g,** G protein binding through α5 helix of mini-$G_{\alpha 13}$ (gold) by GPR56 (blue) and mini-$G_{\alpha o}$ (red) by GPR97 (PDB ID: 7D77, in white) showing substantially greater opening of TM5-6 in the GPR56 TA-bound structure.

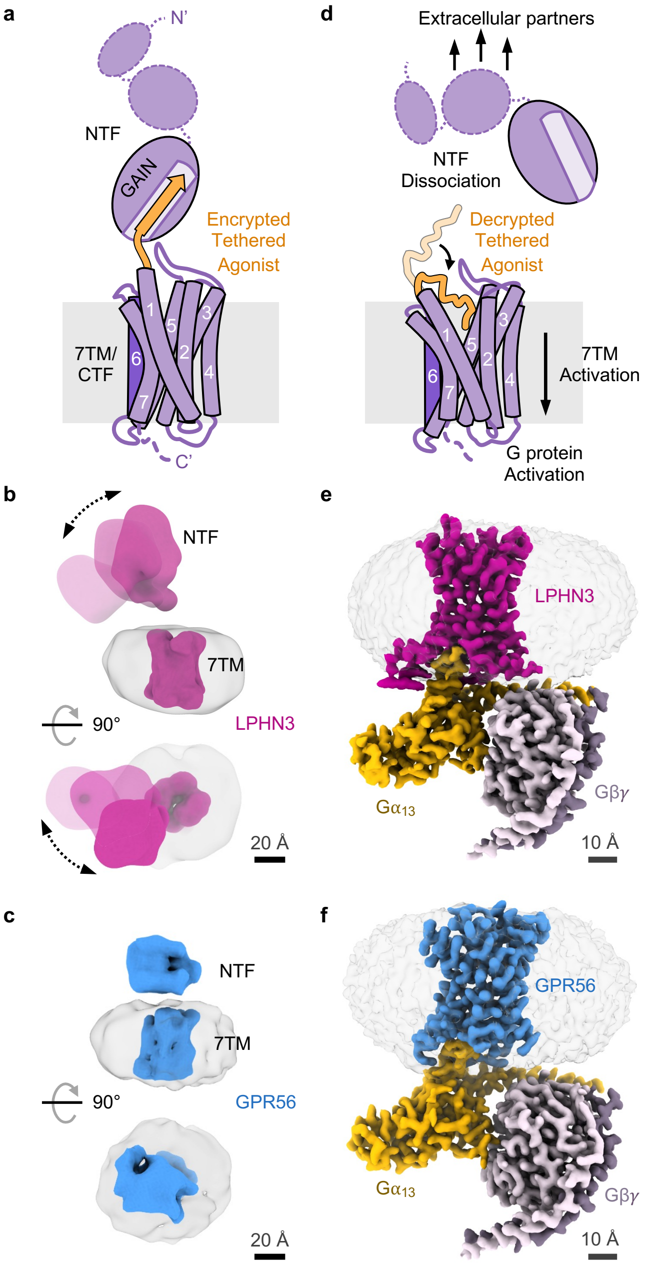
a
N'
NTF
GAIN
Encrypted
Tethered
Agonist
7TM/
CTF
1
2
3
4
5
6
7
C'
d
Extracellular partners
NTF
Dissociation
Decrypted
Tethered
Agonist
7TM
Activation
G protein
Activation
b
NTF
7TM
90°
LPHN3
20 Å
c
NTF
7TM
90°
GPR56
20 Å
e
LPHN3
Gα13
Gβγ
10 Å
f
GPR56
Gα13
Gβγ
10 Å

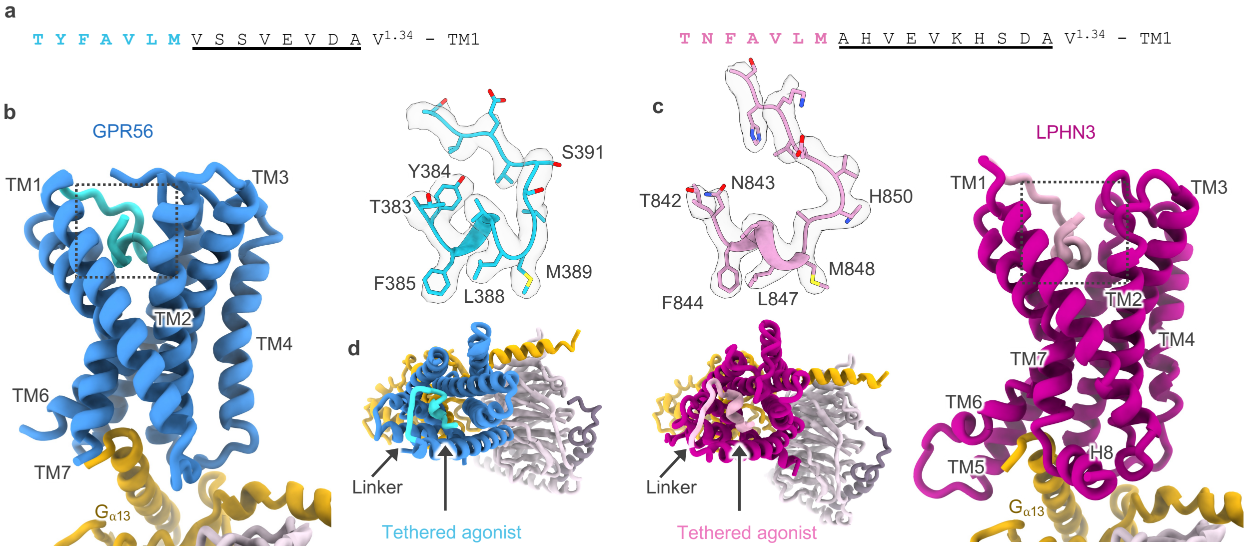
a
T Y F A V L M V S S V E V D A V1.34 - TM1
T N F A V L M A H V E V K H S D A V1.34 - TM1
b
GPR56
TM1
TM3
TM2
TM4
TM6
TM7
Gα13
Y384
T383
S391
F385
L388
M389
c
N843
T842
H850
F844
L847
M848
LPHN3
TM1
TM3
TM2
TM4
TM7
TM6
TM5
H8
Gα13
d
Linker
Tethered agonist
Linker
Tethered agonist

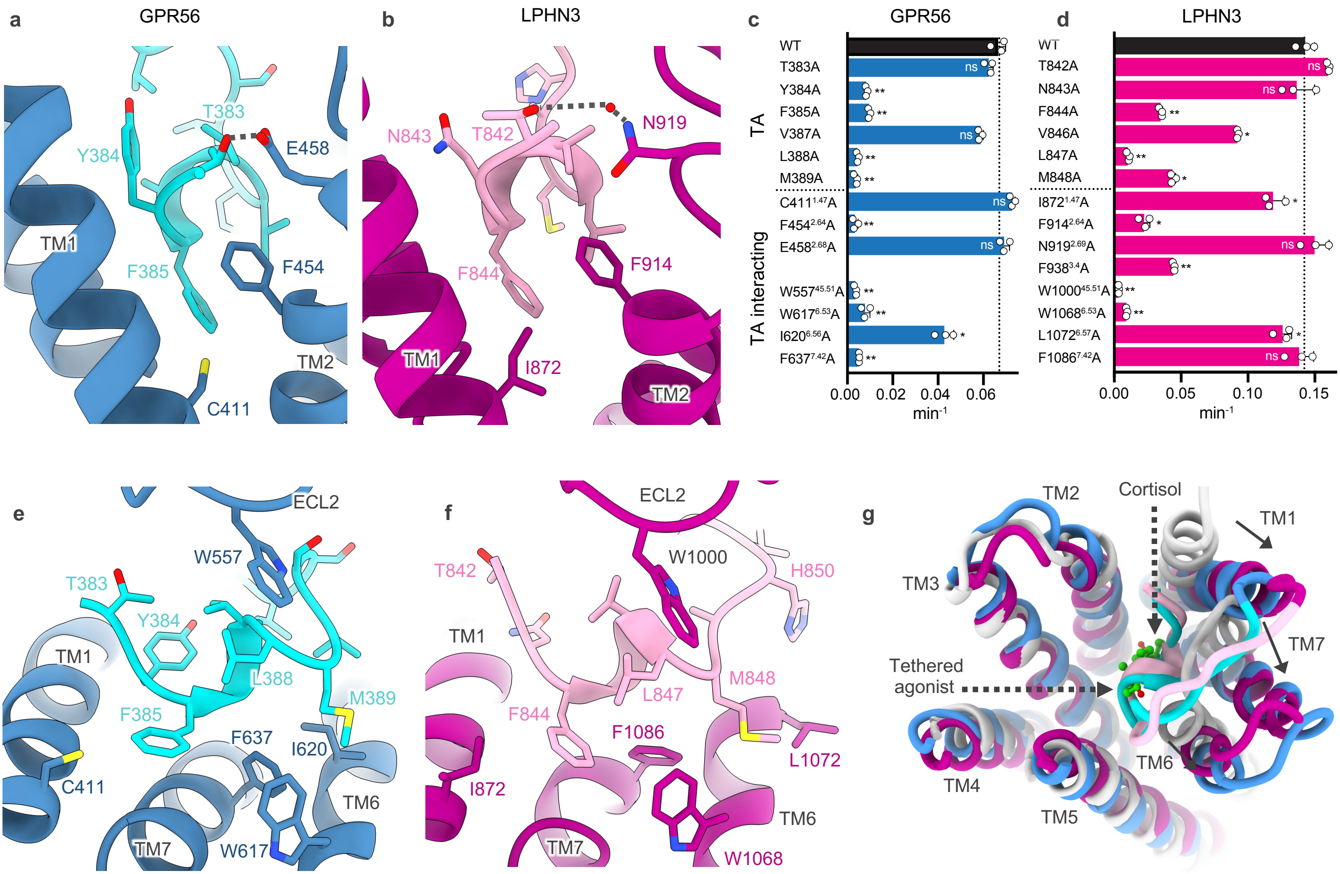
a
GPR56
Y384
T383
E458
TM1
F385
F454
TM2
C411
b
LPHN3
N843
T842
N919
F844
F914
TM1
I872
TM2
c
GPR56
TA
TA interacting
WT
T383A
Y384A
F385A
V387A
L388A
M389A
C411$^{1.47}$A
F454$^{2.64}$A
E458$^{2.68}$A
W557$^{45.51}$A
W617$^{6.53}$A
I620$^{6.56}$A
F637$^{7.42}$A
ns
**
*
0.00
0.02
0.04
0.06
min$^{-1}$
d
LPHN3
WT
T842A
N843A
F844A
V846A
L847A
M848A
I872$^{1.47}$A
F914$^{2.64}$A
N919$^{2.69}$A
F938$^{3.4}$A
W1000$^{45.51}$A
W1068$^{6.53}$A
L1072$^{6.57}$A
F1086$^{7.42}$A
ns
**
*
0.00
0.05
0.10
0.15
min$^{-1}$
e
ECL2
W557
T383
Y384
TM1
L388
M389
F385
F637
I620
C411
TM6
TM7
W617
f
ECL2
W1000
T842
H850
TM1
M848
L847
F844
F1086
L1072
I872
TM6
TM7
W1068
g
TM2
Cortisol
TM1
TM3
TM7
Tethered agonist
TM6
TM4
TM5

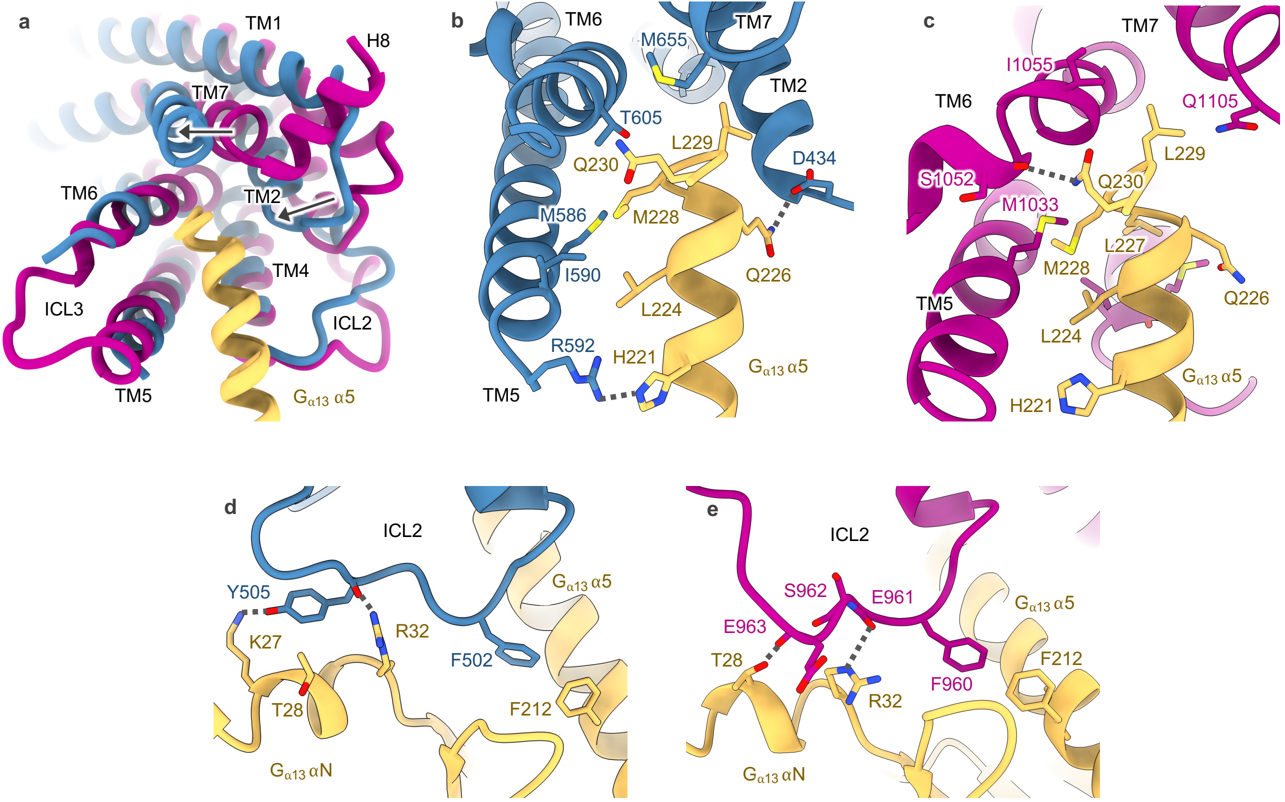
a
TM1
H8
TM7
TM6
TM2
TM4
ICL3
ICL2
TM5
Gα13 α5
b
TM6
M655
TM7
TM2
T605
L229
Q230
D434
M586
M228
I590
Q226
L224
R592
H221
Gα13 α5
TM5
c
TM7
I1055
Q1105
TM6
L229
S1052
Q230
M1033
L227
M228
Q226
TM5
L224
Gα13 α5
H221
d
ICL2
Y505
Gα13 α5
R32
K27
F502
T28
F212
Gα13 αN
e
ICL2
S962
E961
Gα13 α5
E963
T28
F212
F960
R32
Gα13 αN